Analyst

PAPER

Cite this: *Analyst*, 2017, **142**, 1608

Refinement of insulator-based dielectrophoresis†

Claire V. Crowther and Mark A. Hayes*

The ability to separate analytes with increasingly similar properties drives the field of separation science. One way to achieve such separations is using trapping and streaming dielectrophoresis (DEP), which directly exploits the subtle differences in the electrophysical properties of analytes. The non-uniform fields necessary for DEP can be formed using various insulator shapes in microchannels. Current insulator shapes include triangles, diamonds, circles, and rectangles. However, all of these insulators pose problems for trapping, streaming, and sorting (deflection) as the induced fields/gradients are not behaviorally consistent across the lateral dimension. This leads to analytes experiencing different forces depending on their pathline in the microchannel and result in low resolution separations. Based on an iterative process that explored approximately 40 different insulator shapes, a design was chosen that indicated improved particle streamlines, better trapping efficiency, and consistent electrical environments across the lateral dimension. The design was assessed by simulations where the electric field, gradient of the electric field squared, and the ratio of the two were plotted. The improved design includes a unique new multi-length scale element. The multi-length scale structure streamlines the analyte(s) and improves homogeneity in the lateral dimension, while still achieving high gradients necessary for analyte separation using DEP. The design is calculated to keep analytes on the centerline which should improve resolution, and eliminate extraneous trapping zones. Behaviors consistent with the features of the simulations were observed in proof of principle experiments using representative test probes.

Received 21st November 2016,
Accepted 30th March 2017

DOI: 10.1039/c6an02509a

rsc.li/analyst

Introduction

In the last several years the exploitation of microfluidics as a method for analyte manipulation has grown rapidly, particularly for biological samples. This is driven by the limitations of current diagnostic methods, especially their need for large sample volumes, lengthy analysis times, and low resolution/sensitivity. Microfluidic devices have the potential to improve each of these figures of merit and provide increased portability. A wide range of bioparticles can be addressed, including animal cells,[1] organelles,[2] proteins,[3,4] DNA[5–7] and bacteria.[8–11]

One major division of microfluidics uses electrokinetic (EK) and the dielectrophoretic (DEP) forces on particles (molecules are considered particles for the purposes of this discussion). The EK forces allows for the manipulation of both the particle and the suspending medium, as it is the sum of electrophoresis and electroosmosis. DEP is the force, in its purest form, exerted on a polarizable particle present in a non-uniform electric field ($\bar{E}$). Utilizing EK and DEP forces, trapping and streaming of particles is possible. This allows for the separation of analytes based on their specific and subtle electrical physical properties.[10,12–14]

Previous work on DEP separations has utilized electrode-based dielectrophoresis (eDEP), which has the advantage of being able to induce high field gradients with a low applied voltage.[15–22] Fabrication of eDEP devices can be difficult and is sometimes expensive. The electrodes are easily fouled, rendering the channels non-reusable. The electrodes also induce electrolysis, creating bubbles and buffer alteration and the high gradients are limited to local volume near the conductive interface.

Insulator-based dielectrophoresis (iDEP) is an alternative to induce non-uniform electric fields in a microchannel. In contrast to eDEP, the electrodes are placed in distal inlet and outlet reservoirs and the electric field is defined by channel insulators and the conductive media. This resolves many of the issues encountered with eDEP (electrolysis, bubbles, fouling). Both AC and DC fields can be used with iDEP; DC fields drive overall particle movement since it induces EK and DEP transport and AC can refine separations influencing DEP only.[2,6,23–27] iDEP was theoretically conceived and proof of concept established in the early 2000s.[6,28] Since then many different types of insulators have been utilized to achieve points of constriction[29] including single obstacles of various shapes,[30,31] oil menisci,[32,33] and insulating posts.[28,34–36] Work

Arizona State University, School of Molecular Sciences, Mail Stop 1604, Tempe, AZ 85287, USA. E-mail: mhayes@asu.edu; Fax: (+480) 965-2747; Tel: (+480) 965-2566

† Electronic supplementary information (ESI) available: Other insulator shapes tested, trapping condition, videos of experiments. See DOI: 10.1039/c6an02509a

has also been performed using height constrictions in microchannels and presents many unique opportunities for future developments.[37–40] The first separation to be demonstrated using iDEP was that of live and dead bacteria.[9,10]

For all iDEP designs, the constriction geometry defines the overall performance, whether the basic shape is repeated or varies some characteristic dimension. The assessment here focuses on the constriction design, which is universal to all iDEP systems.[29] Examples of insulator shapes currently utilized include rectangle,[14,31,41] triangle,[25–27,31] sawtooth,[11,23,42,43] circular posts,[2,10,11,27,28,35,44] and diamond posts.[28,45,46] Trapping DEP leads to the isolation and concentration of analytes near the constriction points in the microchannels.[1–3,6,8,10,11,25,26,28,35] Separation can be achieved as a bipurification, where one analyte is trapped and other analytes continue to flow through the microchannel,[10] or multiple analytes can be trapped in the same microchannel.[11] Deflection techniques can also be used to achieve separations.[13,47] Separation is possible in this case as the different mobilities of analytes results in different degrees of deflection when the particle passes the point of constriction in the microdevice.[48] Inducing the same behavior for a given particle type across all starting points will improve all existing iDEP systems.

Each of these configurations creates different local environments for the analytes relative to the central longitudinal axis, depending on the initial lateral position in the channel (Fig. 1).[1,49,50] This is true for local traps or elution strategies.

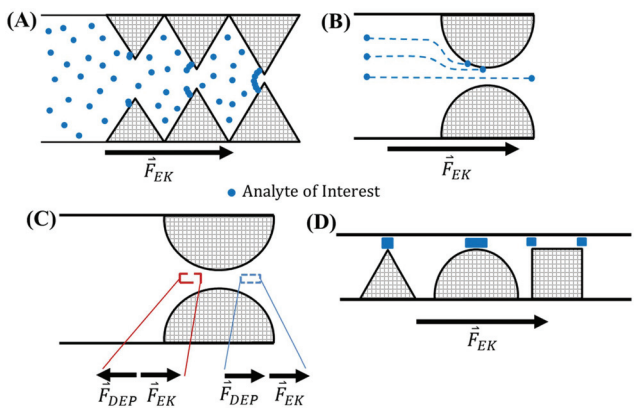

Fig. 1 General illustration showing similar physical processes regardless of insulator geometry. For the purposes of this illustration, the bulk electrokinetic movement ($\vec{F}_{EK}$) for all the channels is from left to right. For (A) and (B) the blue spheres represent a single population of identical particles of interest experiencing negative dielectrophoresis. (A) Typical g-iDEP behavior, where some analytes are trapped near the point of greatest constriction at larger pitches before full cross-section sequestration occurs. (B) Identical particles experience different outcomes depending on initial pathline. In some cases, particles on centerline can traverse the gate, whereas those near the wall will be trapped. This results in like-particles being distributed throughout a range of gate pitches. (C) Near-centerline summation of forces for left-to-right $\vec{F}_{EK}$ and negative dielectrophoresis. (D) Various insulator shapes that are currently used that all allow variation in like-particle behavior depending on initial pathline. Blue rectangles depict the point of strongest DEP interaction for a particle in a DC field.

For the purpose of high resolution separations, several factors come into play; including high values for the electric field and gradient[12] and the induction of all particles of an identical population to traverse the longitudinal axis in a similar fashion where the electric field strength and gradient intensity achieve separatory differentials (whether trapping, streaming (multi-outlet), or stochastic-based and chromatography-like elution-based strategies).[10,11,42,43,51–55] The identical or at least similar (accounting for diffusion and dispersion) movement of all particles of a homogeneous population is a core tenet of separations science. The manipulation of analytes by DEP is possible because each analyte has unique properties reflected by their electrophoretic (μ_{EP}) and dielectrophoretic (μ_{DEP}) mobilities. For all microchannels varying the constriction size, shape of the insulator, suspending medium, or the applied potential will alter the forces and thus the interaction of the particle with the microchannel.[3,43,56] Preliminary work has been performed to improve and optimize the current iDEP designs utilized for trapping DEP.[45,57,58] However, these works only manipulate the dimensions of currently-used shapes, and do not focus on streamlining the analytes thus eliminating extraneous trapping zones to help improve all types of DEP (trapping, deflection, and streaming). Several other works in DC and AC DEP have focused on generating a constant gradient, but these focus on the longitudinal axis or within limited zones of interaction.[59–61] In contrast, this work is aimed at minimizing inhomogeneity across the lateral dimension.

This work seeks to develop a novel insulator geometry to improve the separation capabilities of iDEP. By iterative modeling of current and potential new designs using finite element software, a new multi-length scale insulator has been developed for negative DEP applications. The insulator design is calculated to streamline the particles, minimize the possibility for extraneous trapping zones, laterally homogenize the forces, while maintaining high gradients to allow for separation. Assurance that the models were physical was demonstrated using several experimental test probes.

Theory

Manipulation of the analytes is possible because of the influence of the EK and the DEP forces. Further development can be found in several previous works.[9,10,28,62,63]

The electrokinetic velocity, $\vec{v}_{EK}$, is the combination of electrophoretic and electroosmotic velocities

$$\vec{v}_{EK} = \mu_{EK}\vec{E} = (\mu_{EOF} + \mu_{EP})\vec{E} \quad (1)$$

The DEP velocity, $\vec{v}_{DEP}$, can be represented in terms of dielectrophoretic mobility (μ_{DEP}) and the gradient of the electric field squared, $\nabla|\vec{E}|^2$.[62,64,65]

$$\vec{v}_{DEP} = -\mu_{DEP}\nabla|\vec{E}|^2 \quad (2)$$

Dielectrophoresis describes the force that is exerted on a polarizable particle present in a non-uniform electric

field. For a spherical particle the force is described by the following:[62,65]

$$\vec{F}_{\mathrm{DEP}} = 2\pi\varepsilon_{\mathrm{m}} r^3 f_{\mathrm{CM}} \nabla|\vec{E}|^2 \quad (3)$$

where $\vec{F}_{\mathrm{DEP}}$ is the DEP force, ε_{m} is the permittivity of the medium, r is the radius of the particle, and f_{CM} is the Clausius–Mossotti factor which is dependent on the conductivity of the particle and medium in DC fields. Depending upon the sign of f_{CM}, the particle of interest will either undergo positive or negative DEP. In positive DEP, the conductivity of the particle is greater than the conductivity of the media; meaning that the particle is attracted to areas of high electric field. In negative DEP, the conductivity of the media is larger than that of the particle so the particle is effectively repelled from the locations of high electric field strength.

The flow of analytes in a microfluidic channel is controlled by advection, diffusion and electrokinetic effects.[45] By eliminating pressure driven flow in the system advection can be ignored. For large particles (>1 μm) diffusion can be disregarded. Therefore particle flow, $\vec{j}$, can be described by the following.[46,66]

$$\vec{j} = D\nabla \mathrm{C} + C(\vec{v}_{\mathrm{Bulk}} + \vec{v}_{\mathrm{EK}} + \vec{v}_{\mathrm{DEP}}) \approx C(\vec{v}_{\mathrm{EK}} + \vec{v}_{\mathrm{DEP}}) \quad (4)$$

Where D is the diffusion coefficient, C is the particle concentration, and $\vec{v}_{\mathrm{Bulk}}$ is the motion of the fluid due to pressure driven flow. Therefore, particle flow is consequently only affected by the concentration of the analyte, EK, and DEP.

Dielectrophoretic forces are influenced by constrictions in the microchannel, as this is where the highest gradients are induced. Particle motion can be mostly attributed to EK when the particles are not near points of constriction in the microfluidic device, hence particle movement can be approximated by the electric field lines in these zones (eqn (4)).

Trapping of analytes occurs when the particle velocity along the field line is zero, $\vec{j}\cdot\vec{E} = 0$, such that $\vec{v}_{\mathrm{DEP}}$ is equal to $\vec{v}_{\mathrm{EK}}$. A detailed determination of the trapping condition is included in the ESI.† Trapping of analytes can therefore be described using the EK and DEP mobilities:

$$\left(\mu_{\mathrm{EK}}\vec{E} - \mu_{\mathrm{DEP}}\nabla|\vec{E}|^2\right)\cdot\vec{E} \leq 0 \quad (5)$$

Eqn (7) can be rearranged such that dielectrophoretic trapping is described as:[67]

$$\frac{\nabla|\vec{E}|^2}{E^2}\cdot\vec{E} \geq \frac{\mu_{\mathrm{EK}}}{\mu_{\mathrm{DEP}}} \quad (6)$$

For streaming and sorting DEP the threshold for trapping is never achieved, but the particles are influenced by DEP (eqn (4)).

EK and DEP result in extremely complex systems, however the behavior can be classified as either streaming or trapping behaviors. Trapping behaviors occur when the interaction between the $\vec{E}$ and the slope of $\frac{\nabla|\vec{E}|^2}{E^2}\cdot\vec{E}$ meet at highly acute angles. Streaming DEP occurs where the $\vec{E}$ and the slope of $\frac{\nabla|\vec{E}|^2}{E^2}\cdot\vec{E}$ interact at glancing angles.

Mathematical modeling

Microchannel geometries

Six-constriction microchannels with various insulators were used in this study, where the gate pitch changed after 3 gates, resulting in 2 gate groupings. The gate pitches were 36.37 μm and 34.10 μm (Fig. 2A). The gate pitches were chosen to mimic measurements for a current channel design. The current channel measurements have been used for the manipulation and separation of several analytes including: polystyrene spheres, red blood cells, different serotypes of *Escherichia coli*, and different strains of *Staphylococcus epidermidis*.[1,8,11,42] The channels modeled ranged in length from 7.5–12 mm (only the *Inverse 20× Curve* channels were on the upper end of this). A 500 V potential was applied so that the inlet wall was a ground and the outlet wall carried the potential (Fig. 2A). AutoCAD 2014 (Autodesk, Inc., San Rafael, CA) was used to build the to-scale microchannels.

Insulator geometries were modeled to determine their effects on the local electric potential induced by distal electrodes. The insulator geometries focused on the following features: the effect of sharp features (triangular shape), flat designs (*Inverse 20× Curve* and rectangular insulators), rounded insulators (circular and elliptical shapes), and the addition of small insulator features to larger geometry elements near or at the point of highest constriction (Fig. 2B).

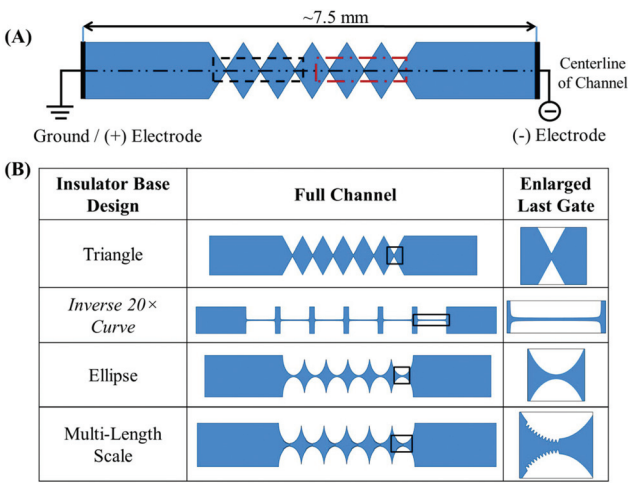

Fig. 2 Illustration of the generalized form of channels investigated computationally. (A) Enlarged sample schematic for one of the iDEP devices modeled. The approximate length of the channel and the constrictions were consistent for all models. The gate pitch of the first three gates is 36.37 μm and 34.10 μm for the second set of three gates. The only exception is for the *Inverse 20× Curve* where the channel was about 12 mm long. (B) Schematics of the some of the various insulator shapes and an enlarged view of the last gate. Other insulator shapes can be found in the ESI.†

Several manipulations to the small insulating features were tested. Examples of these manipulations include: changing the height (*e.g.* 20–30 μm), diminishing the insulator height, in-setting them into the base insulator, changing the width, increasing and decreasing the number of small insulators, altering the distribution of small insulators (over half the top or the full top of the base insulator), changing the shape (triangles, rectangles, curved fins, and ellipses). A sampling of these different geometries can be found in the ESI (Fig. S1 & S2†).

Fabrication limitations were not considered when testing the different variations of the multi-length scale designs. However, the multi-length scale insulator design developed and discussed in this paper was conceived to adhere to follow current fabrication limitations. The photomask has a tolerance for the critical dimension of 0.3 μm ± 10% with a maximum tolerance of 0.6 μm.[68] For the photomask the resolution over a 5.0 cm channel is 1.5 μm.[68] Wafers were made using standard photolithographic techniques; specifically using the photoresist AZ 3312 (AZ Electronic Materials) which can be used to create features less than 0.50 μm.[69] A microchannel depth of 20 μm with minimum feature size of a 2 μm is achievable using a Surface Technology Systems Deep Silicon Etch, which utilizes SF_6, C_4F_8, and O_2 to etch using the Bosch process for an anisotropic etch.[70] Therefore the final multi-length scale insulator shape discussed in this paper was developed with a minimum critical dimension of 2.5 μm.

Finite element multiphysics mathematical models

The distribution of the electric potential was modeled using the finite-element multiphysics simulation software (COMSOL Multiphysics 5.1). The AC/DC module was specifically used to determine the distribution of the $\vec{E}$, $\nabla|\vec{E}|^2$, and $\frac{\nabla|\vec{E}|^2}{E^2}\cdot\vec{E}$.

Two dimensional models of the microchannels were utilized as the electric potential is expected to vary minimally across the channel depth as the channels are relatively shallow compared to the other dimensions of the microchannel.[67] The insulating posts will distort the electric field of the entire depth of the microchannel as they are they full height of the microchannel. The same material properties and element size parameters were used for all microchannels for original comparison. The mesh was refined further for all designs discussed in this paper.

The distribution of the electric potential was determined using the Laplace equation, where the electric potential (φ) within a microchannel is continuous:

$$\nabla^2\varphi = 0 \tag{7}$$

The boundaries are defined as the surfaces of the microchannel and insulators where the boundary conditions applied are as follows:

$$\vec{n}\cdot\vec{J} = 0 \text{ at the boundaries} \tag{8}$$

$$\varphi = V_{\text{inlet}} \tag{9}$$

$$\varphi = V_{\text{oulet}} \tag{10}$$

where $\vec{n}$ is the normal vector from the surface, $\vec{J}$ is the electrical current density, and V_{inlet} and V_{outlet} are the potentials applied at the inlet and outlet of the microchannel.

Materials and methods

Microdevice fabrication

The multi-length scale insulator was developed into two different devices (Analyte and Larger) with varying sizes of gate sizes to achieve $\frac{\nabla|\vec{E}|^2}{E^2}\cdot\vec{E}$ ratios applicable to micron sized analytes. For both microchannels the width and depth were 1000 μm and 19.6 ± 0.7 μm (average between templates), respectively. The microchannels have circular, terminal reservoirs that defined the inlet and the outlet. The length of the microchannels is 3.69 cm and 3.52 cm for the Analyte and Larger designs, respectively. The channels vary based on the differential of the size between gates. The Analyte microchannel has 27 gates, where each gate size is replicated three times with a gate range of 37.01 μm to 12.27 μm. The Larger microchannel has 24 gates, with replicates of three for each gate size, ranging from 20.4 μm to 17.6 μm. The microfluidic devices were fabricated as discussed previously.

Once the template wafers were prepared polydimethylsiloxane (PDMS) (Sylgard 184, Dow/Corning, Midland, MI) was poured on the wafers and cured at 70 °C for one hour. The PDMS casts were peeled from the templates, cut to size, and the terminal reservoirs access points were punched out with a diameter of 3 mm.

The microchannels were assembled by bonding the PDMS to a glass coverplate. Both were treated with oxygen plasma in a plasma cleaner (PDC-32G, Harrick Plasma, Ithaca, NY) for 60 seconds at 18 W. The PDMS and glass coverplate sealed on contact forming the microchannel.

Microparticles and suspending medium

Experiments were performed using two different analytes. Sulfate-modified, 2.0 μm diameter, fluorescent yellow-green (ex/em 505/515) polystyrene spheres (Life Technologies, Eugene, OR) were suspended in DI-water, pH 6.3, to reach a desired particle concentration. 2.7 μm unlabeled silica spheres (Agilent Technologies, Santa Clara, CA) were suspended in 2 mM phosphate buffer, pH 7.4 with 3 mg mL^{-1} bovine serum albumin (BSA). All analytes were vortexed and sonicated before use to disrupt aggregates.

Experimental

Preliminary experiments were performed to ensure general features noted in the simulation were physical. Using an Olympus

IX70 inverted microscope with 4× and 20× objectives, completed microdevices were observed. Approximately 20 μL of the either the polystyrene or silica spheres were pipetted into the inlet reservoir. A similar volume of the suspending solution was added to the outlet reservoir and used to balance pressure driven flow, confirmed by observing the elimination of longitudinal particle motion in the channel. Platinum electrodes with a diameter of 0.404 mm (Alfa Aesar, Ward Hill, MA) were inserted into the reservoirs and connected to a HVS448 3000D high voltage sequencer (Labsmith, Inc., Livermore, CA). The samples were illuminated using a combination of a mercury short arc lamp (H30 102 w/2, OSRAM) and Fiber-Lite High Intensity Illuminator (Model 170D, Dolan Jenner, Lawrence, MA). To observe the fluorescence a Texas Red triple bandpass cube (Olympus, Center Valley, PA) was utilized. A range of DC voltages, ~0–1000 V, were applied across the device and used to manipulate both analytes. For the polystyrene sphere experiments color video was collected using a digital single-lens reflex Nikon D5000 camera (Nikon, Melville, NY). Videos and images of the silica spheres were collected using a monochrome QICAM cooled CCD camera (QImaging, Inc., Surrey, BC) and Streampix V image capture software (Norpix, Inc., Montreal, QC). ImageJ was used for file conversion and to assess, manipulate and quantify the images, and generate data.

Results and discussion

The shape of insulators in iDEP defines the ability to manipulate analytes within the microfluidic channel. The insulator induces the distribution of $\vec{E}$ and therefore the $\nabla|\vec{E}|^2$ and the streaming or trapping of the analyte. For trapping, streaming, and sorting it is desirable for each particle of a given physical makeup to experience the same environment to ensure consistent outcomes. Concurrently, the dielectrophoretic forces must be high enough to overcome transport and diffusional forces to generate an observable effect. This requires large gradients, resulting in large $\nabla|\vec{E}|^2$ values.[1,12]

Depending on the geometric configuration and strength of the various forces, streaming or trapping can result. Sorting of particles in a continuous or semi-continuous mode has been an important use of dielectrophoresis. A common strategy is deflection using streaming DEP, but recent work has shown sorting by exploiting trapping or trapping-like mechanisms.[8,11,13,47] For deflection techniques to operate most efficiently, similar principles apply, in that, all particles of a population should occupy a homogenous lateral environment during the deflection process. This suggests that all particles for each analyte population is influenced by the same $\frac{\nabla|\vec{E}|^2}{E^2}\cdot\vec{E}$ values within each zone throughout the process.

The need for a gradient and to have all analytes experience equivalent forces as they traverse the system can be at odds with one another, by definition gradient means a change in the value where as there needs to be homogeniety in a lateral (or semilateral) dimension. This study probes a large variety of insulator shapes to create an environment where high gradient values are attained, while giving a homogeneous environment to all particles within a given analyte population exposed to the separatory system.

Several geometric constructs were probed, including the effect of different base insulators: triangle, rectangle, *Inverse 20× Curve*, circle, and ellipse (Fig. 3). Furthermore the addition of small insulators to the base structure was tested; variables included the shape of the small insulator(s) (triangle, ellipse, rectangle, and curved fin), number of small insulator(s), location on the base insulator (across the whole top or half, insetting the insulators in the base insulator), and the dimensions of the small insulators (height, width variations at base and top). Examples of these different geometries that were tested can be found in the ESI (Fig. S2†). All of these geometries were eliminated based on one or more of the following factors: not achieving $\nabla|\vec{E}|^2$ values comparable to currently utilized designs, inefficient streaming (presence of local traps) of analytes, and/or severe lateral field inhomogeniety (ESI Table S1†). The multi-length scale insulator design was developed further and was optimized to adhere to the fabrication limitations as noted.

To achieve high $\nabla|\vec{E}|^2$, the most effective insulator design has sharp points, demonstrated by the triangular insulator (Fig. 3C). The radius of curvature of the insulator for sharp features changes rapidly which, in turn, constricts the electric field and results in a high $\nabla|\vec{E}|^2$. The triangular insulator is representative of diamonds, sawteeth, and triangles used for insulators.[11,23,28,31,42,43,45] Along the centerline, the value for the $\nabla|\vec{E}|^2$ for the 34.10 μm gate is approximated to be 3.2×10^{16} V^2 m^{-3}, which is the highest value of any of the insulator shapes examined. Particles will travel along the field line by EK forces in the absence of a significant gradient. However, these sharp features create local dielectrophoretic traps where the electric field line impinges the slope of the local gradient at an acute angle. This is seen at the lateral pathlines away from the centerline for these triangle designs, which are representative of this class of insulator shapes. In cases where trapping does not occur, particles are deflected in a highly non-linear fashion preventing consistent separations *via* deflection and streaming.

Circular insulators have smaller gradients (Fig. 3A & B) as the constriction of the electric field is more gradual as compared to triangular insulators. Therefore only smaller $\nabla|\vec{E}|^2$ values are possible with the same constriction size compared to sharp insulators. The $\nabla|\vec{E}|^2$ along the centerline is 8.8×10^{14} and 1.85×10^{15} V^2 m^{-3} for the circular and ellipse shaped insulators respectively with a gate pitch of 34.10 μm.

Rectangular insulators are also used to alter the gradient of the electric field (Fig. 3D).[14,41] The maximum $\nabla|\vec{E}|^2$ along the centerline is 6.3×10^{14} V^2 m^{-3} with a gate pitch of 34.10 μm. The gradient for rectangular and *Inverse 20× Curve* insulators (Fig. 3D & F) are smaller than for circular and triangular insulators as the constriction of the electric field is abrupt, so a high gradient is limited to the corners of the insulators. These values are the lowest of any insulator shape, this could be

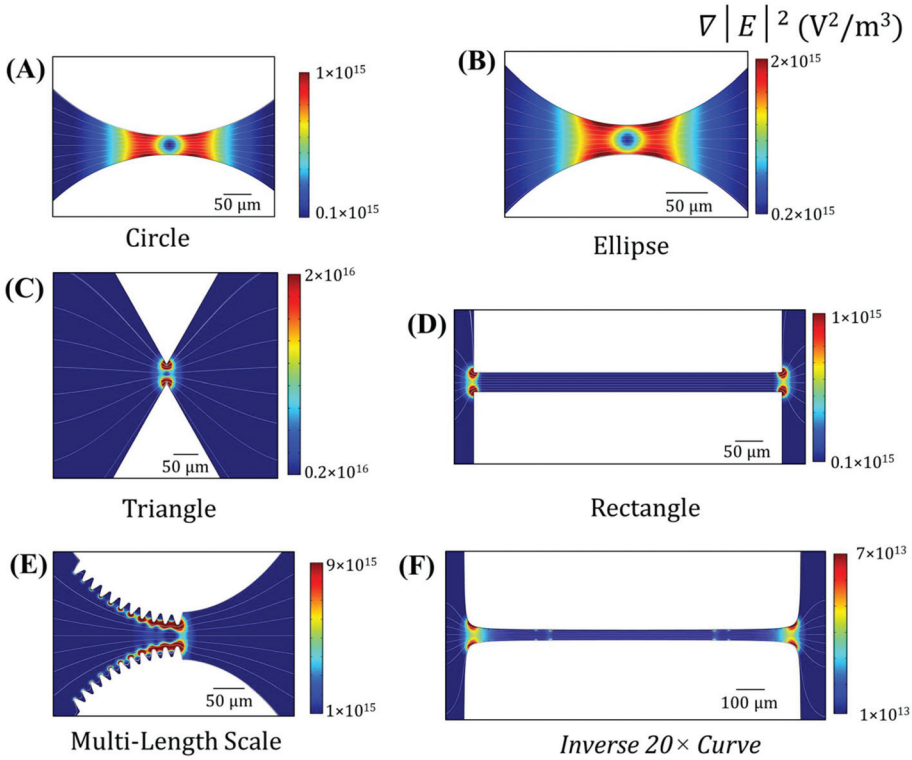

Fig. 3 Study of general design options (others shown in ESI, Fig. S2†). Two dimensional plots of the $\nabla|\vec{E}|^2$ for different insulator shapes with electric field lines (grey). The absolute value for the color scale for each design differs to highlight the patterns that result from the specific insulator shape. Each image is of the first gate of 34.10 μm for the different designs with an applied global potential of 500 V.

increased by shortening the insulator or channel, however the $\nabla|\vec{E}|^2$ will still be lower than the other designs, leading to less influence on the particles in the channel.

The $\nabla|\vec{E}|^2$ value is not the same laterally for the triangular, circular, and rectangular insulators, so that particles will experience different forces based on their initial pathlines. Within each of these designs, particles starting at various vertical positions (as drawn, lateral position relative to the longitudinal axis of the device and applied external electric field) will be trapped at widely varying locations (Fig. 1), meaning that trapping DEP will not occur at the same voltage for the different analyte pathlines.[49,50] The rectangular and *Inverse 20× Curve* have the most laterally homogeneous electric field, however they do not have a strong enough gradient to trap analytes of typical interest.[12] For the case of sorting DEP methods having a low $\nabla|\vec{E}|^2$ will result in lower resolution separations as particles will not be deflected as much. This is compounded by the fact that like-particles along different pathlines will experience different forces, altering their deflection and thus the resolution of the separation. Streaming DEP is also affected by having low $\nabla|\vec{E}|^2$ values, and thus lower DEP forces, therefore the particles are not as effectively streamlined. The effects of inhomogeneous lateral fields are similar to the wall effect in chromatography, which results in lower resolution separations.[71]

The advantage to multi-length scale design is the small insulators alter the distribution of the electric field significantly at the points approaching the constriction resulting in higher values for the $\nabla|\vec{E}|^2$, while the elliptical base minimized lateral heterogeneity. As the particles approach the point of constriction, under conditions of negative DEP, the analytes are pushed towards the center of the microchannel as they are repelled from the small insulators. The most useful insulator design from this study has an elliptically-shaped base insulator and small 20 μm-tall elliptically-shaped insulators across half the top of the base (Fig. 3E). The $\nabla|\vec{E}|^2$ at the 34.10 μm gate pitch is 1.7×10^{15} V^2 m^{-3}. This value is lower than for the triangular insulators and comparable to ellipse insulators, but higher than the other insulators.

All further comparisons made are between a triangular insulator, an elliptical insulator, and the new multi-length scale insulator. The triangular and elliptical insulators represent issues of partial trapping and an inhomogeneous lateral environment present for all other designs (circle and rectangle) and the triangular insulator has the highest $\nabla|\vec{E}|^2$ along the centerline. The elliptical insulator is also used for comparison to determine the effects of the addition of the small insulators for the multi-length insulator. Using the definition of trapping in an iDEP device defined in eqn (6) particles are trapped based on the ratio of the μ_{EK} and μ_{DEP}. Using a known analyte (*Escherichia coli*), an established value for μ_{EK} is -1.0×10^{-8} m^2 V^{-1} s^{-1},[8] noting that the analyte is rod shaped, but this is accounted for in the determination of μ_{EK}. The dielectrophoretic mobility can be calculated

assuming the particle is between 0.1–1.0 μm, using the following relationship.[12]

$$\mu_{DEP} = \frac{\varepsilon_m r^2 f_{CM}}{3\eta} \quad (12)$$

where media permittivity (ε_m) is 10^{-9} F m^{-1}, the radius of the particle (r) is 10^{-6} to 10^{-7} m, f_{CM} is −0.3, and solution viscosity (η) is 10^{-3} Ns m^{-2}.[12] This gives a range for μ_{DEP} of -1.0×10^{-17} to -1.0×10^{-19} m^4 V^{-2} s^{-1}. Therefore a range for the ratio of mobilities is 1.0×10^9 V m^{-2} to 1.0×10^{11} V m^{-2}. These values reasonably coincides with the value determined for *Staphylococcus epidermidis* of $4.6 \pm 0.6 \times 10^9$ V m^{-2} for gentamicin resistant and $9.2 \pm 0.4 \times 10^9$ V m^{-2} for gentamicin sensitive.[11]

A direct visual 2D comparison of $\frac{\nabla|\vec{E}|^2}{E^2}\cdot\vec{E}$ within the three designs provides evidence for significantly different behaviors (Fig. 4). The full range of $\frac{\nabla|\vec{E}|^2}{E^2}\cdot\vec{E}$ values depicts that a triangular insulator achieves the highest values followed by the multi-length scale and then elliptical insulator (Fig. 4A, C & E). In these representations, the intensity of the $\frac{\nabla|\vec{E}|^2}{E^2}\cdot\vec{E}$ value is plotted showing effect on a particle with a various mobility ratios. Specific ratios were utilized as the various shapes with the same constrictions and voltage applied will trap particles with ratios between 5.4×10^9 and 1.7×10^{10} V m^{-2} (Fig. 4B, D & F). The ratios were chosen to depict potential trapping conditions specific to the applied voltage, insulator shape, and gate pitch. A ratio of 5.6×10^9 V m^{-2} was selected for the multi-length scale design selected to show trapping behavior at a slightly narrower gate (right) and complete passage of all particles at the wider gate (left) for the multi-length scale design (Fig. 4F). The color scale toward red is the most repelling environment and the white areas completely exclude analytes with these properties. The portions with color define the area accessible to this analyte. This can be observed by noting that the white area completely bridges the gap on the right gate, indicating excluded area and trapping behavior.

Significantly different behaviors can be deduced for the triangular and ellipse insulators (Fig. 4A–D). For particles off the centerline, the electrokinetic pathlines impinge upon the gradient at an acute angle, allowing for partial trapping at wider gates (Fig. 4B & D). At the top (or bottom) the pathlines clearly impinge on the slope of the $\frac{\nabla|\vec{E}|^2}{E^2}\cdot\vec{E}$ at an acute angle. When full trapping across the gate occurs, an arc forms represented by the left edge of the white areas (Fig. 4B & D). This arc structure has been observed in many experimental systems and is demonstrated computationally (Fig. 5A–D).[1,3,8–11,42,45,49,50] The net result is consistent with current experimental systems,

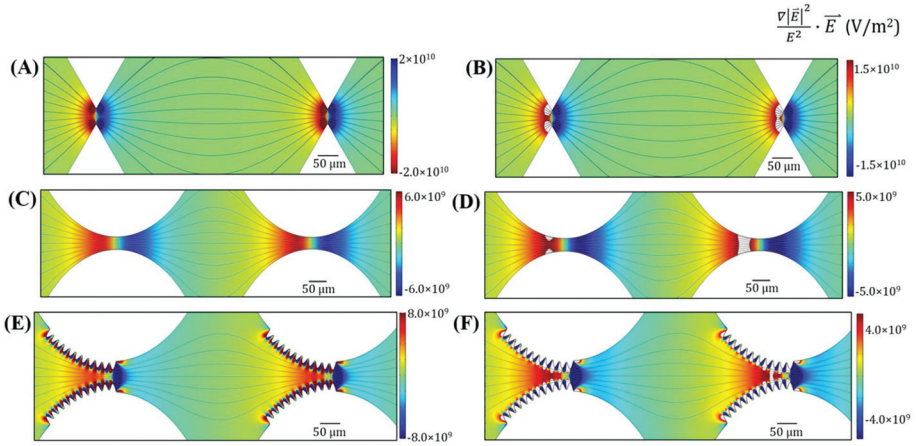

Fig. 4 Study emphasizing differences between triangular, ellipse, and multi-length scale insulators at the critical transition to full trapping at second gate (non-trapping at left, trapping at right, panels B, D, & F). White areas indicate zones where the analyte is completely excluded (see text). Similar data in all six panels, with different representations to emphasize various transport and trapping features. Panels A, C, & E are the full distribution of $\frac{\nabla|\vec{E}|^2}{E^2}\cdot\vec{E}$. Electric field lines present in all panels. Panels B, D, & F illustrates the area that is accessible (colored region) to a particle that would be repelled (negative dielectrophoresis) with a given particle property (μ_{EK}/μ_{DEP}: 1.8×10^{10} V m^{-2} – triangle, 5.4×10^9 V m^{-2} – ellipse, and 5.6×10^9 V m^{-2} – multi-length scale). At low $\frac{\nabla|\vec{E}|^2}{E^2}\cdot\vec{E}$ values, electric field lines are the pathlines of particles. Panels showing triangular insulator (A & B) show electric field lines off the centerline impinging the slope of the $\frac{\nabla|\vec{E}|^2}{E^2}\cdot\vec{E}$ (local direction of dielectrophoretic forces) at highly acute angles, creating a local trapping point. These lateral trapping areas are present at all sharp features and some rounded features (B & D). In this study, for the triangular and ellipse insulator given the analyte μ_{EK}/μ_{DEP} ratio of choice, the analyte is partially trapped at the first gate and fully trapped at the second gate. In contrast, the critical particle would pass the first gate completely and be trapped at the second gate for the multi-length scale insulator. Further, the multi-length scale insulator does not exhibit any lateral traps were the electric field lines impinge the $\frac{\nabla|\vec{E}|^2}{E^2}\cdot\vec{E}$ slope at extremely acute angles. The gate pitches are 36.37 μm and 34.10 μm, left to right with an applied global potential of 500 V (A–F).

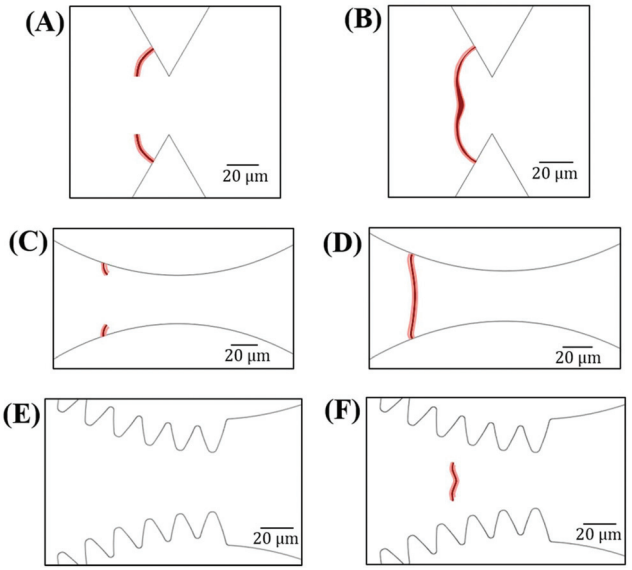

Fig. 5 Depiction of trapping locations for various mobility ratios, where the dark red represents the trapping condition, and the pink is the region surrounding where trapping is also likely to occur. Partial trapping is depicted in A & C, while complete trapping of the analyte is present in B, D & F. The multi-length scale insulator does not have partial trapping as the analytes are deflected to the centerline, and not trapped until the necessary conditions are met. A, C, & E are representative of 36.37 μm gates, while B, D, & F are representative of 34.10 μm gates. The mobility ratios depicted are as follows: A & B – 1.8×10^{10} V m^{-2}, C & D – 5.4×10^{9} V m^{-2}, E & F – 5.6×10^{9} V m^{-2}. All images are modelled such that the applied global potential is 500 V.

where small collections of analytes are observed close to the point of greatest constriction of wide gates and full arcs form when complete trapping across the lateral dimension occurs. For a single particle population, some particles will trap on these wide gates, while other will continue on, which distributes that single population throughout the device.

The reason the multi-length scale system prevents these local traps at wide gates is the slope of the $\frac{\nabla|\vec{E}|^2}{E^2}\cdot\vec{E}$ impinges upon the electrokinetic lines at a glancing angles and simply streams particles that experience negative DEP toward the centerline. For the left, larger, gate particles not on the centerline will be influenced by the gradient near the white space (inaccessible area) first and be deflected towards the centerline, as this interaction does not occur at the highly acute angles necessary for trapping. As the particles interact near an inaccessible area first, and are deflected towards the centerline they will not interrogate the local minima between the small insulators (Fig. 4F). If the centerline trapping forces are insufficient, no trapping occurs at that gate.

Predicted trapping locations for the different designs were determined, based on different mobilities ratio. For both the triangular and elliptically shaped insulators partial trapping is seen at the 36.37 μm gate (Fig. 5A & C), while no trapping is seen for multi-length insulator (Fig. 5F). Complete trapping of an analyte is seen for all insulator shapes at the 34.10 μm gate

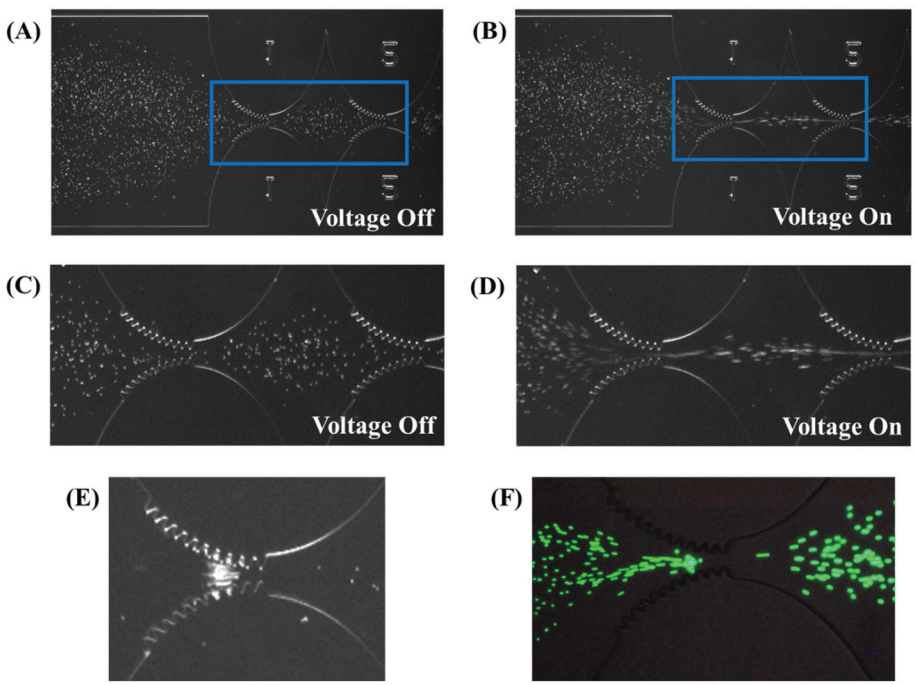

Fig. 6 Examples of trapping and streaming of polystyrene and silica spheres using the multi-length scale insulators. Light field/dark field contrast enhanced image of (A–E) 2.7 μm silica particles. Fluorescence/bright field contrast enhanced image of (F) 2.0 μm yellow-green fluorescent polystyrene spheres. A–D depicts the streaming effect on the analyte with the applied voltage. C & D are enlarged images of the blue rectangles in A & B. With the voltage applied the analyte is pushed to the centerline of the channel and deflected away from the small insulators resulting in more effective streaming. E & F depict that the capture of different analytes is possible and correlates to the predicted capture location from the models. Gate sizes and applied potentials are as follows (A–D) 20.5 μm, –600 V (E) 18.0 μm, –1000 V (F) 18.7 μm, –400 V.

(Fig. 5B, D & F). These results for the common insulator shapes agree with what many groups have seen computationally and experimentally.[9,35,45,67]

One feature which promises improved results beyond the removal of local traps is that the assessable area limits the lateral variation in $\frac{\nabla|\vec{E}|^2}{E^2}\cdot\vec{E}$. At a trapping location (Fig. 5F), the values are relatively constant across the entire gap. This is a direct result of the streamlining such that at the third small tooth (starting at the point of constriction working left) the channel width is 42.80 μm, however the accessible area to the analyte is only about 30 μm (Fig. 5F). The particles are deflected towards the centerline of the channel, such that they will not interrogate the space close to the top or between the small insulators.

The multi-length scale insulator was fabricated and exploratory testing performed using two model analytes, polystyrene and silica spheres. Based on the preliminary results presented in Fig. 6 the model was determined to be physical. This was based on the streaming effect of the analyte depicted in Fig. 6 and ESI Videos.† The analytes are seen to be deflected away from the small insulators and pushed towards the centerline of the channel, (Fig. 6A–D). This ensures that the analytes will experience more similar forces as the analytes follow more similar pathlines. Looking at Fig. 6E & F both analytes are trapped at the third tooth (starting at the point of constriction working left), which reflects what was predicted in the model (Fig. 5F).

For the separation of mixed samples, the effect of analytes that experience positive DEP must be considered as they will be drawn to the drown-stream side of the small elliptical insulators. This is represented by the dark blue regions in Fig. 4F. This may result in unwanted behavior including clogging, distortion of forces, particle–particle interactions, *etc.* It is important to note that the majority of the analytes that experience positive DEP theoretically would be trapped at the preliminary gates in the microchannel and would therefore not influence separations at later gates. Some potential ways to address this concern would be by including a primary wide gate that would trap all the analytes that experience positive DEP, allowing for the separation of analytes that experience negative DEP in the rest of the microchannel. Additionally, to prevent clogging, the introduction of side channels may allow for the drain off desired analytes, including those that experience positive DEP.

For sorting and streaming techniques, in the region particles are predicted to interrogate, the forces are more uniform laterally with the multi-length scale insulator meaning that the particles will be repelled or deflected in more a similar manner as they will experience more similar forces. This lays the framework for the possibility of higher resolution separations as particles are deflected the same amount and better streaming will occur as the particles will be confined to a smaller area in the channel than with the other designs.

Conclusion

The development of a new multi-length scale insulator for iDEP insulator streamlines the analytes to ensure that like-particles experience similar environments as the $\vec{E}$ is more homogenous in the accessible area. This should minimize partial and extraneous trapping. The two factors are predicted to improve separation for both deflection and trapping techniques. Preliminary experimental evidence is consistent with the model and this claim. This can all be accomplished while maintaining $\frac{\nabla|\vec{E}|^2}{E^2}\cdot\vec{E}$ values high enough to accomplish trapping.

Conflict of interest

The authors declare no competing financial interest.

Abbreviations

(DEP)	Dielectrophoresis
(iDEP)	Insulator-based dielectrophoresis
(g-iDEP)	Gradient insulator-based dielectrophoresis
(EP)	Electrophoresis
(EO)	Electroosmosis
(μ_{EK})	Electrokinetic mobility
(μ_{EP})	Electrophoretic mobility
(μ_{EO})	Electroosmotic mobility
(μ_{DEP})	Dielectrophoretic mobility
(f_{CM})	Clausius–Mossotti factor
($\vec{v}_{EK}$)	Electrokinetic velocity
($\vec{v}_{DEP}$)	Dielectrophoretic velocity
($\vec{E}$)	Electric field strength
($\nabla\|\vec{E}\|^2$)	Dielectrophoretic gradient factor

Acknowledgements

The authors acknowledge the facilities and staff at the Center for Solid State Electronic Research (CSSER) for assistance with microfluidic fabrication. This work was supported by National Institutes of Health grants 1R03AI094193-01, 1R03AI099740-01, and R03AI111361-01.

References

1 P. V. Jones, S. J. R. Staton and M. A. Hayes, *Anal. Bioanal. Chem.*, 2011, **401**, 2103–2111.
2 J. Luo, B. G. Abdallah, G. G. Wolken, E. A. Arriaga and A. Ros, *Biomicrofluidics*, 2014, **8**, 021801.
3 S. J. R. Staton, P. V. Jones, G. Ku, S. D. Gilman, I. Kheterpal and M. A. Hayes, *Analyst*, 2012, **137**, 3227–3229.

4 A. Nakano, F. Camacho-Alanis and A. Ros, *Analyst*, 2015, **140**, 860–868.
5 M. Washizu and O. Kurosawa, *IEEE Trans. Ind. Appl.*, 1990, **26**, 1165–1172.
6 C.-F. Chou, J. O. Tegenfeldt, O. Bakajin, S. S. Chan, E. C. Cox, N. Darnton, T. Duke and R. H. Austin, *Biophys. J.*, 2002, **83**, 2170–2179.
7 R. Martinez-Duarte, F. Camacho-Alanis, P. Renaud and A. Ros, *Electrophoresis*, 2013, **34**, 1113–1122.
8 P. V. Jones, A. F. DeMichele, L. Kemp and M. A. Hayes, *Anal. Bioanal. Chem.*, 2014, **406**, 183–192.
9 B. H. Lapizco-Encinas, B. A. Simmons, E. B. Cummings and Y. Fintschenko, *Anal. Chem.*, 2004, **76**, 1571–1579.
10 B. H. Lapizco-Encinas, B. A. Simmons, E. B. Cummings and Y. Fintschenko, *Electrophoresis*, 2004, **25**, 1695–1704.
11 P. V. Jones, S. H. Hilton, P. E. Davis, R. Yanashima, R. McLemore, A. McLaren and M. A. Hayes, *Analyst*, 2015, **140**, 5152–5161.
12 P. V. Jones and M. A. Hayes, *Electrophoresis*, 2015, **36**, 1098–1106.
13 B. G. Abdallah, T.-C. Chao, C. Kupitz, P. Fromme and A. Ros, *ACS Nano*, 2013, **7**, 9129–9137.
14 S. K. Srivastava, J. L. Baylon-Cardiel, B. H. Lapizco-Encinas and A. R. Minerick, *J. Chromatogr. A*, 2011, **1218**, 1780–1789.
15 M. P. Hughes, H. Morgan, F. J. Rixon, J. P. H. Burt and R. Pethig, *Biochim. Biophys. Acta, Gen. Subj.*, 1998, **1425**, 119–126.
16 J. S. Crane and H. A. Pohl, *J. Electrochem. Soc.*, 1968, **115**, 584–586.
17 H. A. Pohl and J. S. Crane, *Biophys. J.*, 1971, **11**, 711–727.
18 K. F. Hoettges, M. P. Hughes, A. Cotton, N. A. E. Hopkins and M. B. McDonnell, *IEEE Eng. Med. Biol. Mag.*, 2003, **22**, 68–74.
19 J. Johari, Y. Hübner, J. C. Hull, J. W. Dale and M. P. Hughes, *Phys. Med. Biol.*, 2003, **48**, N193.
20 H. Morgan, M. P. Hughes and N. G. Green, *Biophys. J.*, 1999, **77**, 516–525.
21 M. P. Hughes and H. Morgan, *Anal. Chem.*, 1999, **71**, 3441–3445.
22 M. P. Hughes, *Electrophoresis*, 2002, **23**, 2569–2582.
23 K. P. Chen, J. R. Pacheco, M. A. Hayes and S. J. R. Staton, *Electrophoresis*, 2009, **30**, 1441–1448.
24 V. Chaurey, C. Polanco, C.-F. Chou and N. S. Swami, *Biomicrofluidics*, 2012, **6**, 012806.
25 N. Swami, C.-F. Chou, V. Ramamurthy and V. Chaurey, *Lab Chip*, 2009, **9**, 3212–3220.
26 Y.-H. Su, M. Tsegaye, W. Varhue, K.-T. Liao, L. S. Abebe, J. A. Smith, R. L. Guerrant and N. S. Swami, *Analyst*, 2014, **139**, 66–73.
27 A. Gencoglu, F. Camacho-Alanis, V. T. Nguyen, A. Nakano, A. Ros and A. R. Minerick, *Electrophoresis*, 2011, **32**, 2436–2447.
28 E. B. Cummings and A. K. Singh, *Anal. Chem.*, 2003, **75**, 4724–4731.
29 S. Srivastava, A. Gencoglu and A. Minerick, *Anal. Bioanal. Chem.*, 2011, **399**, 301–321.
30 S. S. Keshavamurthy, K. M. Leonard, S. C. Burgess and A. R. Minerick, *NSTI-Nanotech*, Boston, MA, 2008, pp. 401–404.
31 Y. Kang, D. Li, S. Kalams and J. Eid, *Biomed. Microdevices*, 2008, **10**, 243–249.
32 I. Barbulovic-Nad, X. Xuan, J. S. H. Lee and D. Li, *Lab Chip*, 2006, **6**, 274–279.
33 P. K. Thwar, J. J. Linderman and M. A. Burns, *Electrophoresis*, 2007, **28**, 4572–4581.
34 B. H. Lapizco-Encinas, R. V. Davalos, B. A. Simmons, E. B. Cummings and Y. Fintschenko, *J. Microbiol. Methods*, 2005, **62**, 317–326.
35 P. Sabounchi, A. Morales, P. Ponce, L. Lee, B. Simmons and R. Davalos, *Biomed. Microdevices*, 2008, **10**, 661–670.
36 J. Regtmeier, T. T. Duong, R. Eichhorn, D. Anselmetti and A. Ros, *Anal. Chem.*, 2007, **79**, 3925–3932.
37 W. A. Braff, A. Pignier and C. R. Buie, *Lab Chip*, 2012, **12**, 1327–1331.
38 W. A. Braff, D. Willner, P. Hugenholtz, K. Rabaey and C. R. Buie, *PLoS One*, 2013, **8**, e76751.
39 L. M. Barrett, A. J. Skulan, A. K. Singh, E. B. Cummings and G. J. Fiechtner, *Anal. Chem.*, 2005, **77**, 6798–6804.
40 P. Zellner, T. Shake, Y. Hosseini, D. Nakidde, M. V. Riquelme, A. Sahari, A. Pruden, B. Behkam and M. Agah, *Electrophoresis*, 2015, **36**, 277–283.
41 K. H. Kang, Y. Kang, X. Xuan and D. Li, *Electrophoresis*, 2006, **27**, 694–702.
42 S. J. R. Staton, K. P. Chen, T. J. Taylor, J. R. Pacheco and M. A. Hayes, *Electrophoresis*, 2010, **31**, 3634–3641.
43 M. D. Pysher and M. A. Hayes, *Anal. Chem.*, 2007, **79**, 4552–4557.
44 R. C. Gallo-Villanueva, C. E. Rodríguez-López, R. I. Díaz-de-la-Garza, C. Reyes-Betanzo and B. H. Lapizco-Encinas, *Electrophoresis*, 2009, **30**, 4195–4205.
45 A. LaLonde, A. Gencoglu, M. F. Romero-Creel, K. S. Koppula and B. H. Lapizco-Encinas, *J. Chromatogr. A*, 2014, **1344**, 99–108.
46 E. B. Cummings, *IEEE Eng. Med. Biol. Mag.*, 2003, **22**, 75–84.
47 S. K. Srivastava, A. Artemiou and A. R. Minerick, *Electrophoresis*, 2011, **32**, 2530–2540.
48 B. G. Abdallah, S. Roy-Chowdhury, J. Coe, P. Fromme and A. Ros, *Anal. Chem.*, 2015, **87**, 4159–4167.
49 R. C. Gallo-Villanueva, M. B. Sano, B. H. Lapizco-Encinas and R. V. Davalos, *Electrophoresis*, 2014, **35**, 352–361.
50 M. A. Saucedo-Espinosa and B. H. Lapizco-Encinas, *Electrophoresis*, 2015, **36**, 1086–1097.
51 J. C. Giddings, *Unified Separation Science*, John Wiley & Sons, Inc., New York, 1991.
52 K. J. Morton, K. Loutherback, D. W. Inglis, O. K. Tsui, J. C. Sturm, S. Y. Chou and R. H. Austin, *Proc. Natl. Acad. Sci. U. S. A.*, 2008, **105**, 7434–7438.
53 L. R. Huang, E. C. Cox, R. H. Austin and J. C. Sturm, *Science*, 2004, **304**, 987–990.
54 M. Streek, F. Schmid, T. T. Duong and A. Ros, *J. Biotechnol.*, 2004, **112**, 79–89.

55 A. Ros, W. Hellmich, J. Regtmeier, T. T. Duong and D. Anselmetti, *Electrophoresis*, 2006, **27**, 2651–2658.
56 S. Ozuna-Chacón, B. H. Lapizco-Encinas, M. Rito-Palomares, S. O. Martínez-Chapa and C. Reyes-Betanzo, *Electrophoresis*, 2008, **29**, 3115–3122.
57 G. R. Pesch, L. Kiewidt, F. Du, M. Baune and J. Thöming, *Electrophoresis*, 2016, **37**, 291–301.
58 M. A. Saucedo-Espinosa and B. H. Lapizco-Encinas, *J. Chromatogr. A*, 2015, **1422**, 325–333.
59 N. G. Weiss, P. V. Jones, P. Mahanti, K. P. Chen, T. J. Taylor and M. A. Hayes, *Electrophoresis*, 2011, **32**, 2292–2297.
60 P. H. Humble, R. T. Kelly, A. T. Woolley, H. D. Tolley and M. L. Lee, *Anal. Chem.*, 2004, **76**, 5641–5648.
61 D. J. Allen, R. P. Accolla and S. J. Williams, *Electrophoresis*, 2017, DOI: 10.1002/elps.201600517.
62 H. A. Pohl, *Dielectrophoresis: the behavior of neutral matter in nonuniform electric fields*, Cambridge University Press, Cambridge, New York, 1978.
63 R. Pethig, *Biomicrofluidics*, 2010, **4**, 022811.
64 R. F. Probstein, *in Physicochemical Hydrodynamics: An Introduction*, John Wiley & Sons, Inc., 1994, pp. 1–8.
65 T. B. Jones, *Electromechanics of Particles*, Cambridge University Press, 1995.
66 J.-S. Kwon, J.-S. Maeng, M.-S. Chun and S. Song, *Microfluid. Nanofluid.*, 2008, **5**, 23–31.
67 J. L. Baylon-Cardiel, B. H. Lapizco-Encinas, C. Reyes-Betanzo, A. V. Chavez-Santoscoy and S. O. Martinez-Chapa, *Lab Chip*, 2009, **9**, 2896–2901.
68 J. Dingley, *JD Photo-Tools: The Photo–Mask Guide*, 2014, pp. 1–89.
69 AZ Electronic Materials: AZ® 3300 Series Crossover Photoresists, 2005.
70 J. Bhardwaj, H. Ashraf and A. McQuarrie, Proc. Symp. Microstructures and Microfabricated Systems, ECS, 1997.
71 R. A. Shalliker, B. S. Broyles and G. Guiochon, *J. Chromatogr. A*, 2000, **888**, 1–12.